PCCP

PAPER

View Article Online
View Journal

Cite this: DOI: 10.1039/c6cp01723a

Organic–inorganic interactions of single crystalline organolead halide perovskites studied by Raman spectroscopy†

Li-Qiang Xie,‡[a] Tai-Yang Zhang,‡[b] Liang Chen,‡[a] Nanjie Guo,[b] Yu Wang,[a] Guo-Kun Liu,[a] Jia-Rui Wang,[a] Jian-Zhang Zhou,[a] Jia-Wei Yan,[a] Yi-Xin Zhao,*[b] Bing-Wei Mao*[a] and Zhong-Qun Tian[a]

Received 14th March 2016,
Accepted 7th June 2016

DOI: 10.1039/c6cp01723a

www.rsc.org/pccp

Organolead halide perovskites exhibit superior photoelectric properties, which have given rise to the perovskite-based solar cells whose power conversion efficiency has rapidly reached above 20% in the past few years. However, perovskite-based solar cells have also encountered problems such as current–voltage hysteresis and degradation under practical working conditions. Yet investigations into the intrinsic chemical nature of the perovskite material and its role on the performance of the solar cells are relatively rare. In this work, Raman spectroscopy is employed together with CASTEP calculations to investigate the organic–inorganic interactions in $CH_3NH_3PbI_3$ and $CH_3NH_3PbBr_{3-x}Cl_x$ perovskite single crystals with comparison to those having ammonic acid as the cations. For Raman measurements of $CH_3NH_3PbI_3$, a low energy line of 1030 nm is used to avoid excitation of strong photoluminescence of $CH_3NH_3PbI_3$. Raman spectra covering a wide range of wavenumbers are obtained, and the restricted rotation modes of CH_3–NH_3^+ embedded in $CH_3NH_3PbBr_3$ (325 cm^{-1}) are overwhelmingly stronger over the other vibrational bands of the cations. However, the band intensity diminishes dramatically in $CH_3NH_3PbBr_{3-x}Cl_x$ and most of the bands shift towards high frequency, indicating the interaction with the halides. The details of such an interaction are further revealed by inspecting the band shift of the restricted rotation mode as well as the C–N, NH_3^+ and CH_3 stretching of the $CH_3NH_3^+$ as a function of Cl composition and length of the cationic ammonic acids. The results show that the $CH_3NH_3^+$ interacts with the PbX_3^- octahedral framework via the NH_3^+ end through N^+–H···X hydrogen bonding whose strength can be tuned by the composition of halides but is insensitive to the size of the organic cations. Moreover, an increase of the Cl content strengthens the hydrogen bonding and thus blueshifts the C–N stretching bands. This is due to the fact that Cl is more electronegative than Br and an increase of the Cl content decreases the lattice constant of the perovskite. The findings of the present work are valuable in understanding the role of cations and halides in the performance of $MAPbX_3$-based perovskite solar cells.

Introduction

Solar cells based on organolead halide perovskite have received unprecedented attention since the first report on the liquid perovskite-based dye sensitized solar cell in 2009.[1–6] Rapid and substantial increases of power conversion efficiency (PCE) of solid-state perovskite solar cells with considerable durability have been achieved above 20%,[6–8] making the perovskite-based solar cell promising for practical applications. The superior performance of the perovskite solar cells benefit from the unique structural and electronic properties of the perovskite materials associated with high optical absorption coefficient and ambipolar conductivity.[9,10] For the typical halide perovskite $CH_3NH_3PbI_3$ ($MAPbI_3$) with a tetragonal phase at room temperature, the MA^+ cations are located in the interstices of the PbI_3^- octahedral framework. Although the cations do not directly contribute to the formation of the valence and conduction band structure,[11,12] their orientation and thus the created dipole in the framework are closely related to the dielectricity[13] and ferro-/antiferroelectricity of the perovskite,[14–16] while their rotation can lower the exciton binding energy of perovskites and favor

[a] State Key Laboratory of Physical Chemistry of Solid Surfaces, Department of Chemistry, College of Chemistry and Chemical Engineering, iChEM, Xiamen University, Xiamen 361005, China. E-mail: bwmao@xmu.edu.cn
[b] School of Environmental Science and Engineering, Shanghai Jiao Tong University, 800 Dongchuan Road, Shanghai 200240, China. E-mail: yixin.zhao@sjtu.edu.cn

† Electronic supplementary information (ESI) available. See DOI: 10.1039/c6cp01723a

‡ These authors contributed equally.

the separation and transportation of electrons and holes.[17] Depending on the size, geometry and the embedding manner of the cations, distortion of the octahedral framework can occur, which affects the spatial symmetry and thermal stability of the perovskite structure. Recent studies on the current–voltage hysteresis present severely in planar structured perovskite solar cells have shown that molecular level ferroelectricity[14,18,19] and migration[20–22] of the cations[23,24] under an external electric field may be responsible although the exact origins are still under debate.[25] In any case, cation migration would be detrimental to and lead to the degradation of the solar cell.[23] Hence the role of the cations in the perovskites is two-folded: on the one hand, cation dipole and rotation will modify the electronic structure and lower the exciton energy, which are desirable for good photovoltaic performance; on the other hand, the distortion of the octahedral framework and the migration of the cation can cause undesirable instability of the crystal structure. As a result, it brings the opportunity to improve the photovoltaic performance of the solar cell by optimizing the geometry and chemical structure of the cations.

It is important to note that the behavior of the cations in the inorganic framework is strongly dependent on the micro-environment of organic–inorganic interactions, and investigation on the interactions between the MA^+ and the PbI_3^- in the octahedral framework would in turn be beneficial for understanding the cation influence on the performance of the solar cells. The research into this aspect is emerging and becoming hot topic in the last couple of years. Vibrational spectroscopies including IR[26–28] and Raman,[27,29–33] neutron diffraction[17,34] and NMR[35] have been employed together with theoretical calculations,[11,13,27,36] focusing on the cation dynamics in the lattice by analyzing the rotational and vibrational modes of the cations. A number of Raman spectroscopic studies on $MAPbI_3$ have been reported,[27,29–33] but are mostly limited to the low wavenumber region associated with lattice dynamics of $MAPbI_3$.[29–33] The Raman spectrum covering a wide range of wavenumbers has been obtained only for the orthorhombic γ phase of $MAPbI_3$ at 100 K.[27] Although the information obtained from these Raman spectroscopic investigations have helped in identifying the chemical composition of the perovskite and elucidating the structure and stability of the perovskite, the lack of high wavenumber spectra in most of the studies and the observation of the rotation mode in the low wavenumber region as suggested by the work of neutron diffraction[17,33] hinder the detailed analysis of cation interactions with the microenvironment of the inorganic framework. (We note that during the preparation of this manuscript there appears a paper on Raman spectroscopic study on $MAPbI_3$ and several Br and Cl substituted perovskites covering a wide range of wavenumbers[37].) Moreover, all of the Raman spectroscopic studies reported so far were carried out on planar or mesostructured films, and the quality of the perovskites and thus the quality of Raman spectra can vary diversely depending on the preparation conditions. This poses difficulties for quantitative analysis and comparisons of results among different perovskites and different groups.

In this work, we present a systematic Raman spectroscopic study on the organic–inorganic interactions using single crystalline halide perovskites. Single crystal perovskites have fewer defects in the bulk, which are expected to ensure the best achievable photoelectric properties of the perovskite.[38–40] In addition, they are more stable against water, oxygen and photo-induced heating. Use of single crystalline perovskites would enable Raman spectroscopic investigations in the absence of the interference from structural disorder, which is beneficial to data analysis and comparisons. In the framework of this paper, we perform a comparative wide-range wavenumber Raman spectroscopic investigation on single crystalline $MAPbI_3$, $MAPbBr_3$ and $MAPbBr_{3-x}Cl_x$ perovskites to understand the orientation and rotation behaviors of the MA^+ cation and the interactions of the MA^+ cation with the PbX_3^- anions. A theoretical calculation of the Raman spectrum of MABr powder is performed to guide in the assignment of the Raman bands. Finally, the investigation of halide perovskites with ammonic acid of varying length as the cations is carried out to further elucidate the role of cations.

Experimental

Materials

The following chemicals were used as received: methylammonium iodide ($\geq$99.5%), methylammonium bromide ($\geq$99.5%), lead iodide (PbI_2) (99.999%), lead bromide ($PbBr_2$), γ-butyrolactone (GBL), and DMF were purchased from Sigma-Aldrich while amino acids were from Aladdin Industrial Inc. The $MAPbBr_{3-x}Cl_x$ single crystals were synthesized by heating the DMF precursor solution containing $PbBr_2$ and $[(1-x)CH_3NH_3Br + xCH_3NH_3Cl]$ at 50 °C for several hours as reported previously.[41] For the synthesis of $MAPbI_3$, 1.23 M PbI_2 and MAI were dissolved in GBL at 50 °C. After being fully dissolved, the solution was heated to 100 °C overnight to grow single crystals. Ammonic acid based perovskites were prepared by spin-coating the precursor solution of ammonic acid bromide and $PbBr_2$ at a molar ratio of 2 : 1 onto a cleaned FTO glass at a speed of 6000 rpm for 15 s.

Spectroscopic measurements

UV-vis absorption spectra were recorded on a Cary 5000 UV-VIS-NIR-spectrometer. A photoluminescence spectrum was measured on an XPLORA Raman instrument using a 638 nm excitation line. Raman measurements were conducted on an XPLORA Raman spectrometer (Jobin-Yvon, France) with excitation lines of 532 and 638 nm depending on the use. Laser power density was ca.1.5 and 2.1 mW for 532 and 638 nm, respectively. Optical grating of 1200 T was used. For Raman measurements of $MAPbI_3$ single crystals, an inspector 1030 instrument purchased from SciapsDeltaNu (America) was employed. The Raman spectra of perovskite single crystals were recorded in dry air while those of ammonic acid based perovskite films were protected by argon in a closed cell.

Calculation details for Raman spectra of MABr solid

All the structural optimization and energy calculations were carried out by the CASTEP module in Materials Studios 7.0 as a licensed product of BIOVIA. The MABr structure was constructed

on the basis of the crystal structures and adjusted to follow the C_{2v} symmetry in a primitive cell of *C*-centred orthorhombic lattice. The built structure was fully optimized using the generalized gradient approximation treated by the Perdew–Burke–Ernzerhof potential. Norm-conserving pseudopotentials were used and represented in reciprocal space. The self-consistent field (SCF) procedure was used with a convergence threshold of 10^{-5} au on the energy and electron density. Geometry optimizations were performed with a convergence threshold of 0.03 eV Å^{-1} on the max force, 0.05 Gpa on the max stress, and 0.001 Å on the max displacement. Energy cutoff was set to be 700 eV, and the Brillouin zone was sampled by $3 \times 3 \times 2$ *k*-points using the Monkhorst–Pack scheme. Raman intensities were calculated based on the crystal system type and fitted to a Lorentzian distribution to generate the spectra.

Results and discussion

The $MAPbI_3$ perovskite has a tetragonal structure with an optical absorption coefficient reaching up to 10^4 cm^{-1} in the wavelength range from 400 to 750 nm. Fig. S1 (ESI†) shows photographs of different kinds of $MAPbX_3$ perovskite single crystals in which $MAPbI_3$ appears in dark black color as a result of the strong optical absorption of the high quality single crystals. The UV-vis absorption spectrum and photoluminescence (PL) of a solution-grown $MAPbI_3$ single crystal are shown in Fig. 1A, and it can be seen that the absorption edge extends to around 800 nm, which coincides with the photoluminescence maximum and would result in a strong fluorescence background on Raman spectra in the visible region. Even if a 532 nm laser, which is far from the PL maximum, is used, the strong fluorescence can still be excited, making it difficult to obtain a sufficient signal-to-noise ratio for Raman measurements. Furthermore, the green 532 nm laser has higher energy, which is easier to cause the degradation of perovskite into PbI_2. For this reason, the Raman spectra of the MA^+ in the perovskite have been rarely reported previously. To overcome such problems, we used 1030 nm laser excitation for the Raman study of the $MAPbI_3$ single crystal. High signal-to-ratio Raman spectra covering a wavenumber range from 150 to 2450 cm^{-1} are obtained as shown in Fig. 1B (red line). For comparison, the Raman spectrum of the MAI powder is also provided (black line). Most of the Raman bands of MA^+ on the spectrum of $MAPbI_3$ also appear in the spectrum of the MAI powder, except 275 and 1250 cm^{-1}.

The bands at 914, 989, 1460, 1540 and 1604 cm^{-1} of the MAI powder are all red-shifted to 909, 956, 1426, 1469, and 1583 cm^{-1}, respectively, in the $MAPbI_3$ crystal, which suggests that the MA^+ cation in $MAPbI_3$ interacts strongly with the inorganic PbI_3^- framework, not only by electrostatic attractions but also by chemical interactions, which induces the chemical Stark effect. This chemical interaction between the organic cation and the inorganic framework will be discussed in detail by Raman analysis of $MAPbBr_{3-x}Cl_x$ later. The low frequency band at 275 cm^{-1} is related to the restricted rotation of the MA^+ in $MAPbI_3$. It is known that the free MA^+ rotates fast at room temperature but the rotation mode is Raman and IR inactive. However, for the embedded MA^+ in the $MAPbI_3$, it experiences unequal environment during rotation, which breaks the average crystal symmetry of the PbI_3^- octahedral framework so that the rotation mode becomes Raman active under a restricted condition. Chen *et al.*[17] investigated MA^+ rotation dynamics of $MAPbI_3$ in orthorhombic, tetragonal and cubic phases by an elastic and quasi-elastic neutron scattering technique. They concluded that at room temperature the tetragonal phase MA^+ in the cage of the PbI_3^- framework exhibits four-fold rotational symmetry of the C–N axis (C4 mode) and three-fold rotation around the C–N axis (C3 mode). On the other hand, Brivio *et al.* predicted based on first-principles lattice dynamics that the rotation mode of the CH_3 unit against the NH_3 unit in the tetragonal $MAPbI_3$ is around 300 cm^{-1} at room temperature. But this band was not observed in their Raman experiments even at 100 K, excited by the 785 nm laser. In the present work, the restricted rotation of the MA^+ appears at 275 cm^{-1}, in agreement with the calculated one by Brivio *et al.*, and therefore we attribute the band to the restricted rotation of the CH_3 unit against the NH_3 unit around the C–N axis (*i.e.* the C3 mode noted by Chen *et al.*[17]).

In order to investigate the nature of the organic–inorganic interaction in $MAPbX_3$ perovskites and its impact on the stability and degradation of perovskites, we performed Raman experiments together with theoretical calculations on the

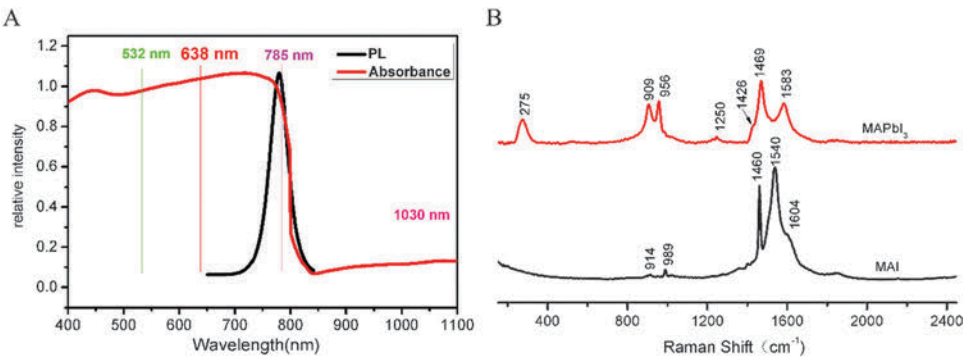

Fig. 1 (A) UV-visible absorption spectrum (red line) and photoluminescence (PL, black line); (B) Raman spectra of CH_3NH_3I powder and $MAPbI_3$ single crystals.

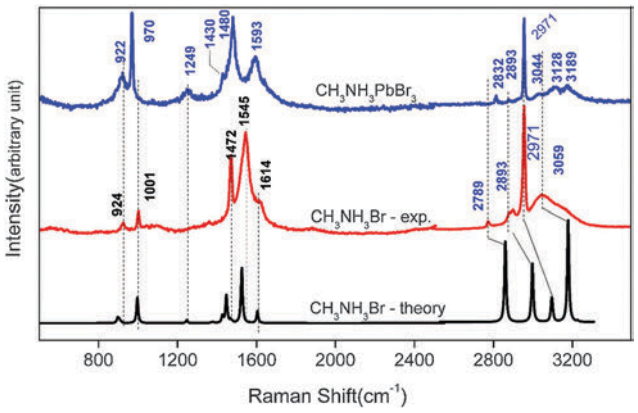

Fig. 2 The measured Raman spectra of CH_3NH_3Br (red line) and the $CH_3NH_3PbBr_3$ single crystal (blue line) and the Raman spectrum calculated by CASTEP in a level of GGA, PBE, DNPs, and $3 \times 3 \times 2$ k-points (black line).

$MAPbBr_3$ single crystal and its precursors. Fig. 2 shows the Raman spectra of the $MAPbBr_3$ single crystal (blue line) and MABr powder (red line) in the region 500–3500 cm^{-1}. A similar chemical Stark effect occurs when the MA^+ is embedded into the $PbBr_3^-$ framework. Also given is the calculated Raman spectrum of the MABr solid (black line), which agrees well with the experimentally measured one in terms of the band number and position. Detailed assignments and analysis of the bands related to MA^+ in MABr and thus in the $MAPbBr_3$ single crystal are provided in Table 1.

In the intermediate wavenumber region of the spectrum of $MAPbBr_3$, the sharp and intense bands at 970 and 1480 cm^{-1} are from the C–N stretching and NH_3^+ asymmetric bending, respectively. They are significantly red-shifted compared to those in the MABr powder sample, which serves as an indication of strong interaction from the inorganic framework. However, the two rocking modes at 922 and 1249 cm^{-1} only show slight yet opposite trends of frequency variation compared with the calculated ones. Moreover, the clearly observed rocking mode at 1249 cm^{-1} and the twisting mode (NH_3^+) at 1593 cm^{-1} in the single crystal $MAPbBr_3$ perovskite are either too weak to be detected or appear as a weak shoulder in the MABr powder. This indicates that the vibrational modes of the MA^+ cation are highly sensitive to the microenvironment.

In the high wavenumber region, the $\nu_{sym}(CH_3)$ at 2893 and $\nu_{asym}(CH_3)$ at 2971 do not shift for the embedded MA^+ while the $\nu_{sym}(N^+–H)$ at 2832 cm^{-1} is blue-shifted and the broad $\nu_{sym}(NH_3^+)$ at 3059 cm^{-1} in the MABr power splits into 3044, 3128, 3189 cm^{-1} in the $MAPbBr_3$ crystal, exhibiting the red or blueshift compared to the MABr powder as shown in Table 1. In other words, the chemical interactions between the organic cation and the inorganic framework take place through the NH_3^+ end of the MA^+. The splitting of the $\nu_{sym}(NH_3^+)$ at 3059 cm^{-1} is most likely due to the hydrogen bonding with the halides in the form of $N^+–H\cdots X$.

To clarify the cation–halide interaction, we performed Raman measurements on $MAPbBr_{3-x}Cl_x$ (x = 0, 0.25, 0.33, 0.5) single crystals. Raman spectra are shown in Fig. 3A, and we focus on and correlate the restricted rotation of MA^+ in the low wavenumber region and the stretching of C–N in the high wavenumber region and their dependency on halides. For the $MAPbBr_3$ single crystal, the MA^+ restricted rotation mode at 325 cm^{-1} is overwhelmingly stronger over the other bands in the whole spectral region. Note that this mode is not observed in $PbBr_2$ and CH_3NH_3Br, as shown in Fig. S3 (ESI†), excluding the possibility of the band arising from the lattice liberation given that the lattice liberation in $MAPbBr_3$ and $PbBr_2$ would appear with a similar Raman shift if any.

It is seen that doping with Cl as low as x = 0.25 substantially diminishes the intensity of the MA^+ restricted rotation mode, while the intensity of the other bands remains almost unchanged; and the band shift from 325 cm^{-1} of the $MAPbBr_3$ single crystal to 333 cm^{-1} of $MAPbBr_{2.5}Cl_{0.5}$ single crystals (Fig. 3B). The same trend for the blueshift is found for the C–N stretching and NH_3^+ twisting of MA^+ from 970 and 1592 cm^{-1} in $MAPbBr_3$ to 973 and 1597 cm^{-1} in $MAPbBr_{2.5}Cl_{0.5}$, respectively. Nevertheless, the Raman shift of the C–H stretching mode changes only slightly from 2971 cm^{-1} in $MAPbBr_3$ to 2972 cm^{-1} in $MAPbBr_{2.5}Cl_{0.5}$. This means that halides play the role in the change of the microenvironment of the PbX_3^- framework, and the bands associated with NH_3^+ are more sensitive to the inorganic microenvironment *via* hydrogen bonding of $N^+–H\cdots X$. The blueshift of the C–N stretching and NH_3^+ twisting observed in the present work agrees with the result obtained from the IR spectroscopic study of Glaser *et al.* It was reported that there exists medium to strong hydrogen

Table 1 The measured Raman shift of vibrational modes of the MABr powder and the $MAPbBr_3$ single crystal. The corresponding assignments are done based on comparisons with those calculated ones for the MABr solid and between the measurements. Symbols ν_1 to ν_{12} are identified according to ref. 42. Detailed illustration of each mode is available in Fig. S4 (ESI)

CASTEP calculation of CH_3NH_3Br	CH_3NH_3Br	$MAPbBr_3$	Peak assignment	Shift after embedding
899	924	922	ν_{12}, $CH_3NH_3^+$ rocking	Red
996	1001	970	ν_5, C–N stretching	Red
1252	—	1249	ν_u, CH_3–NH_3^+ rocking	—
1447	1472	1430	ν_3, sym. NH_3^+ bending	Red
1525	1545	1480	ν_s, asym. NH_3^+ bending	Red
1604	1614	1593	NH_3^+ twisting	—
2877	2789	2832	N^+–H stretching	Blue
3011	2893	2893	ν_2, sym. CH_3 stretching	Not shift
3109	2971	2971	ν_g, asym. CH_3 stretching	Not shift
3188	3059	Split into 3044 312S 3189	ν_1, NH_3*sym. stretching	Split

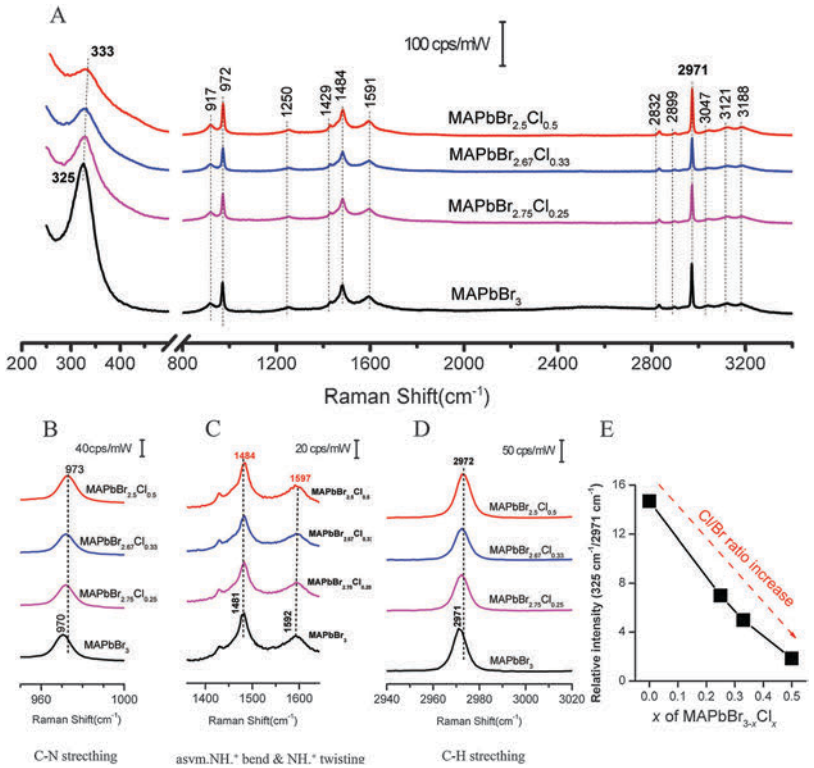

Fig. 3 Raman spectra of $MAPb_{3-x}Cl_x$ single crystals in full range (A) and of the C–N stretching mode (B), asym. NH_3^+ bending and NH_3^+ twisting (C), C–H stretching (D), and the relative intensity of the 325 cm^{-1} band with different Cl contents (E).

bonding in $MAPbX_3$ (X = Cl, Br, I) perovskites at room temperature, but surprisingly the bonding strength differs little among the three halide perovskites.[25] Here the blueshift of the C–N stretching mode of MA^+ indicates the strengthening of the Cl interaction because Cl is more electronegative than Br and doping of Cl is accompanied by the reduction of lattice constant of the perovskite.[41]

As for the influence of the cation size on the restricted rotation, an increase of the cation size by simple addition of more methyl units is expected to increase the activation energy of C4 mode substantially while maintaining that of C3 mode less affected. In other words, the band frequency would remain almost unchanged if a C3 rotation mode is involved in the present work. To study the cation effect, perovskites having ammonic acid as the cations are employed for Raman measurements. These perovskites were synthesized using MABr and alkyl ammonic acid with different carbon chain lengths, *i.e.*, 3C for β-alanice, 4C for aminobutyric acid and 5C for aminovaleric acid, whose molecular structures are shown in Fig. 4B. We mention that when the cation size becomes larger,[43] the 2D-structured perovskites expressed in the formula of A_2MX_4 are formed but the perovskite connectivity (through corner sharing) is still retained.[44] Nevertheless, the ammonic acid cations still interact with the $PbBr_3^-$ framework *via* the NH_3^+ end. Fig. 4A shows the Raman spectra of the ammonic acid-based perovskites. We find that the restricted rotational band around 325 cm^{-1} observed for $MAPbBr_3$ remains almost unchanged after replacing the MA^+ with the ammonic acid regardless of its length. This excludes

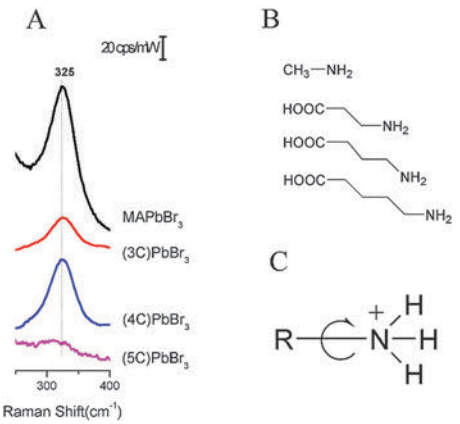

Fig. 4 (A) Raman spectra and perovskite films of different ammonic acids (3C = β-alanice, 4C = aminobutric acid, 5C = aminovaleric acid). (B) Molecular structure of MA and ammonic acid. (C) Schematic of rotation of RNH_3^+ after forming perovskites.

the C4 mode and thus confirms the observed band at 325 cm^{-1} to be the C3 type of the restricted rotation mode in the present work.

These results suggest that the hydrogen bonding between the amine group and the halides in the perovskite structure (N^+–H···X) governs the organic–inorganic chemical interplay, and thus dictates the three-fold rotation dynamics of the organic cation along the C–N axis. This hydrogen bonding together with the cation–anion electrostatic attraction makes

up the overall organic–inorganic interaction in these perovskites. This explains why the band gap and photovoltaic performance of halide perovskites can be successively tuned by varying the composition of the mixed cation/anion perovskites.[6,45] For $MAPbI_3$, the MA^+ might be slightly smaller if measured by the tolerance factor for best perovskites. Thus use of a larger cation like $HC[NH_2]_2^+$ or partially replacing I by Br or Cl can somehow strengthen the overall organic–inorganic interaction and thus improves the stability of these perovskite materials. The current–voltage hysteresis is observed in most of $MAPbI_3$ based perovskite solar cells but greatly reduced in $MAPbBr_3$ based perovskite solar cells.[46] While ferroelectric effects due to the existence of oriented MA domains under applied bias have been suggested,[14,16,18] Beilsten-Edmands *et al*. have recently reported non-ferroelectric nature of the conductance hysteresis in $MAPbI_3$ perovskite-based photovoltaic devices.[25,47] Despite the debates, the proposed restricted rotation of the MA^+ cation upon doping of the Cl^- is in favor of the opinion of the cation involvement of the current–voltage hysteresis in $MAPbX_3$ perovskite solar cells.

Conclusions

We have studied organic–inorganic interactions of halide perovskites by systematic Raman spectroscopic measurements on $MAPbI_3$ and $MAPbBr_{3-x}Cl_x$ single crystals in comparison to those having ammonic acid as the cations. An overall red shift of the Raman bands of MA^+ is observed in $MAPbI_3$ perovskite compared with that in the MAI powder, indicating chemical interactions between MA^+ and PbI_3^-. The restricted rotation mode of CH_3–NH_3^+ is confirmed to be the C3 type along the C–N axis. The intensity of this mode in the $MAPbBr_3$ single crystals is overwhelmingly stronger than the other bands of the cations, but diminishes dramatically with a slight shift towards high wavenumber upon increased doping of Cl^- in $MAPbBr_{3-x}Cl_x$. On the other hand, while the C–N stretching shows a slight band shift, the stretching of CH_3 is affected by neither the doping of Cl^- nor the replacement of cations with the ammonic acid of varying length. These results lead to a conclusion that the interactions of the organic cation with the inorganic PbX_3^- framework are fulfilled mainly *via* the NH_3^+ end through N^+–H$\cdots$X hydrogen bonding. The strength of the interaction can be tuned by the composition of halides but is insensitive to the size of the organic cation. Moreover, doping of Cl^- with higher electronegativity strengthens the hydrogen bonding. The present work has demonstrated that Raman spectroscopic measurements can provide fingerprint information about the details of the organic–inorganic interactions of perovskites, while the use of the single crystals of perovskites improves the quality of Raman spectra and is beneficial to accurate data analysis and comparisons.

Acknowledgements

BWM and ZQT acknowledge the support of the MOST (Grant 2012CB932902) and the NSFC (21473147, 21321062). YZ acknowledges the support of the NSFC (Grant 51372151 and 21303103). LQX, TYZ and LC contributed equally. The authors are grateful to Prof. De-Yin Wu and Mr Zi-Ang Nan at Xiamen University for valuable discussions.

References

1 A. Kojima, K. Teshima, Y. Shirai and T. Miyasaka, *J. Am. Chem. Soc.*, 2009, **131**, 6050–6051.
2 H. S. Kim, C. R. Lee, J. H. Im, K. B. Lee, T. Moehl, A. Marchioro, S. J. Moon, R. Humphry-Baker, J. H. Yum, J. E. Moser, M. Gratzel and N. G. Park, *Sci. Rep.*, 2012, **2**, 591.
3 J. Burschka, N. Pellet, S. J. Moon, R. Humphry-Baker, P. Gao, M. K. Nazeeruddin and M. Gratzel, *Nature*, 2013, **499**, 316–319.
4 M. Z. Liu, M. B. Johnston and H. J. Snaith, *Nature*, 2013, **501**, 395–398.
5 W. Chen, Y. Wu, Y. Yue, J. Liu, W. Zhang, X. Yang, H. Chen, E. Bi, I. Ashraful, M. Grätzel and L. Han, *Science*, 2015, **350**, 944–948.
6 D. P. McMeekin, G. Sadoughi, W. Rehman, G. E. Eperon, M. Saliba, M. T. Hörantner, A. Haghighirad, N. Sakai, L. Korte, B. Rech, M. B. Johnston, L. M. Herz and H. J. Snaith, *Science*, 2016, **351**, 151–155.
7 H. Zhou, Q. Chen, G. Li, S. Luo, T.-b. Song, H.-S. Duan, Z. Hong, J. You, Y. Liu and Y. Yang, *Science*, 2014, **345**, 542–546.
8 W. S. Yang, J. H. Noh, N. J. Jeon, Y. C. Kim, S. Ryu, J. Seo and S. I. Seok, *Science*, 2015, **348**, 1234–1237.
9 G. C. Xing, N. Mathews, S. Y. Sun, S. S. Lim, Y. M. Lam, M. Gratzel, S. Mhaisalkar and T. C. Sum, *Science*, 2013, **342**, 344–347.
10 S. D. Stranks, G. E. Eperon, G. Grancini, C. Menelaou, M. J. P. Alcocer, T. Leijtens, L. M. Herz, A. Petrozza and H. J. Snaith, *Science*, 2013, **342**, 341–344.
11 Y. Wang, T. Gould, J. F. Dobson, H. Zhang, H. Yang, X. Yao and H. Zhao, *Phys. Chem. Chem. Phys.*, 2014, **16**, 1424–1429.
12 F. Brivio, K. T. Butler, A. Walsh and M. van Schilfgaarde, *Phys. Rev. B: Condens. Matter Mater. Phys.*, 2014, **89**, 155204.
13 W.-J. Yin, J.-H. Yang, J. Kang, Y. Yan and S.-H. Wei, *J. Mater. Chem. A*, 2015, **3**, 8926–8942.
14 J. M. Frost, K. T. Butler, F. Brivio, C. H. Hendon, M. van Schilfgaarde and A. Walsh, *Nano Lett.*, 2014, **14**, 2584–2590.
15 H.-S. Kim, S. K. Kim, B. J. Kim, K.-S. Shin, M. K. Gupta, H. S. Jung, S.-W. Kim and N.-G. Park, *J. Phys. Chem. Lett.*, 2015, **6**, 1729–1735.
16 J. M. Frost, K. T. Butler and A. Walsh, *APL Mater.*, 2014, **2**, 081506.
17 T. Chen, B. J. Foley, B. Ipek, M. Tyagi, J. R. D. Copley, C. M. Brown, J. J. Choi and S.-H. Lee, *Phys. Chem. Chem. Phys.*, 2015, **17**, 31278–31286.
18 Z. Xiao, Y. Yuan, Y. Shao, Q. Wang, Q. Dong, C. Bi, P. Sharma, A. Gruverman and J. Huang, *Nat. Mater.*, 2014, **14**, 193–198.
19 S. Liu, F. Zheng, N. Z. Koocher, H. Takenaka, F. Wang and A. M. Rappe, *J. Phys. Chem. Lett.*, 2015, **6**, 693–699.
20 Y. Zhao, C. Liang, H. Zhang, D. Li, D. Tian, G. Li, X. Jing, W. Zhang, W. Xiao, Q. Liu, F. Zhang and Z. He, *Energy Environ. Sci.*, 2015, **8**, 1256–1260.

21 E. L. Unger, E. T. Hoke, C. D. Bailie, W. H. Nguyen, A. R. Bowring, T. Heumuller, M. G. Christoforo and M. D. McGehee, *Energy Environ. Sci.*, 2014, **7**, 3690–3698.
22 H. J. Snaith, A. Abate, J. M. Ball, G. E. Eperon, T. Leijtens, N. K. Noel, S. D. Stranks, J. T.-W. Wang, K. Wojciechowski and W. Zhang, *J. Phys. Chem. Lett.*, 2014, **5**, 1511–1515.
23 M. Bag, L. A. Renna, R. Y. Adhikari, S. Karak, F. Liu, P. M. Lahti, T. P. Russell, M. T. Tuominen and D. Venkataraman, *J. Am. Chem. Soc.*, 2015, **137**, 13130–13137.
24 B. Wu, K. Fu, N. Yantara, G. Xing, S. Sun, T. C. Sum and N. Mathews, *Adv. Energy Mater.*, 2015, **5**, 1500829.
25 J. Beilsten-Edmands, G. E. Eperon, R. D. Johnson, H. J. Snaith and P. G. Radaelli, *Appl. Phys. Lett.*, 2015, **106**, 173502.
26 T. Glaser, C. Müller, M. Sendner, C. Krekeler, O. E. Semonin, T. D. Hull, O. Yaffe, J. S. Owen, W. Kowalsky, A. Pucci and R. Lovrinčić, *J. Phys. Chem. Lett.*, 2015, **6**, 2913–2918.
27 F. Brivio, J. M. Frost, J. M. Skelton, A. J. Jackson, O. J. Weber, M. T. Weller, A. R. Goñi, A. M. A. Leguy, P. R. F. Barnes and A. Walsh, *Phys. Rev. B: Condens. Matter Mater. Phys.*, 2015, **92**, 144308.
28 A. A. Bakulin, O. Selig, H. J. Bakker, Y. L. A. Rezus, C. Müller, T. Glaser, R. Lovrincic, Z. Sun, Z. Chen, A. Walsh, J. M. Frost and T. L. C. Jansen, *J. Phys. Chem. Lett.*, 2015, **6**, 3663–3669.
29 S. T. Ha, X. Liu, Q. Zhang, D. Giovanni, T. C. Sum and Q. Xiong, *Adv. Opt. Mater.*, 2014, **2**, 838–844.
30 B.-w. Park, S. M. Jain, X. Zhang, A. Hagfeldt, G. Boschloo and T. Edvinsson, *ACS Nano*, 2015, **9**, 2088–2101.
31 C. Quarti, G. Grancini, E. Mosconi, P. Bruno, J. M. Ball, M. M. Lee, H. J. Snaith, A. Petrozza and F. De Angelis, *J. Phys. Chem. Lett.*, 2013, **5**, 279–284.
32 M. Ledinsky, P. Loeper, B. Niesen, J. Holovsky, S.-J. Moon, J.-H. Yum, S. De Wolf, A. Fejfar and C. Ballif, *J. Phys. Chem. Lett.*, 2015, **6**, 401–406.
33 R. Gottesman, L. Gouda, B. S. Kalanoor, E. Haltzi, S. Tirosh, E. Rosh-Hodesh, Y. Tischler, A. Zaban, C. Quarti, E. Mosconi and F. De Angelis, *J. Phys. Chem. Lett.*, 2015, **6**, 2332–2338.
34 A. M. A. Leguy, J. M. Frost, A. P. McMahon, V. G. Sakai, W. Kockelmann, C. Law, X. Li, F. Foglia, A. Walsh, B. C. O'Regan, J. Nelson, J. T. Cabral and P. R. F. Barnes, *Nat. Commun.*, 2015, **6**, 7124.
35 R. E. Wasylishen, O. Knop and J. B. Macdonald, *Solid State Commun.*, 1985, **56**, 581–582.
36 F. Zheng, L. Z. Tan, S. Liu and A. M. Rappe, *Nano Lett.*, 2015, **15**, 7794–7800.
37 R. G. Niemann, A. G. Kontos, D. Palles, E. I. Kamitsos, A. Kaltzoglou, F. Brivio, P. Falaras and P. J. Cameron, *J. Phys. Chem. C*, 2016, **120**, 2509–2519.
38 Q. Dong, Y. Fang, Y. Shao, P. Mulligan, J. Qiu, L. Cao and J. Huang, *Science*, 2015, **347**, 967–970.
39 D. Shi, V. Adinolfi, R. Comin, M. Yuan, E. Alarousu, A. Buin, Y. Chen, S. Hoogland, A. Rothenberger, K. Katsiev, Y. Losovyj, X. Zhang, P. A. Dowben, O. F. Mohammed, E. H. Sargent and O. M. Bakr, *Science*, 2015, **347**, 519–522.
40 Y. Liu, Z. Yang, D. Cui, X. Ren, J. Sun, X. Liu, J. Zhang, Q. Wei, H. Fan, F. Yu, X. Zhang, C. Zhao and S. Liu, *Adv. Mater.*, 2015, **27**, 5176–5183.
41 T. Zhang, M. Yang, E. E. Benson, Z. Li, J. van de Lagemaat, J. M. Luther, Y. Yan, K. Zhu and Y. Zhao, *Chem. Commun.*, 2015, **51**, 7820–7823.
42 N. Meinander, S. Forss and G. Bergstrom, *J. Raman Spectrosc.*, 1981, **11**, 155–167.
43 Y. Fang, Q. Dong, Y. Shao, Y. Yuan and J. Huang, *Nat. Photonics*, 2015, **9**, 679–686.
44 D. B. Mitzi, *Chem. Mater.*, 1996, **8**, 791–800.
45 C. Yi, J. Luo, S. Meloni, A. Boziki, N. Ashari-Astani, C. Graetzel, S. M. Zakeeruddin, U. Roethlisberger and M. Graetzel, *Energy Environ. Sci.*, 2016, **9**, 656–662.
46 J. Shi, X. Xu, H. Zhang, Y. Luo, D. Li and Q. Meng, *Appl. Phys. Lett.*, 2015, **107**, 163901.
47 X. Zheng, B. Chen, C. Wu and S. Priya, *Nano Energy*, 2015, **17**, 269–278.